symmetry

MDPI

Article

Analysis of Heat Transfer of Mono and Hybrid Nanofluid Flow between Two Parallel Plates in a Darcy Porous Medium with Thermal Radiation and Heat Generation/Absorption

Moh Yaseen [1], Sawan Kumar Rawat [2], Anum Shafiq [3], Manoj Kumar [1] and Kamsing Nonlaopon [4,*]

[1] Department of Mathematics, Statistics and Computer Science, G.B. Pant University of Agriculture and Technology, Pantnagar 263145, India
[2] Department of Mathematics, KIET Group of Institutions, Delhi-NCR, Meerut Road (NH-58), Ghaziabad 201206, India
[3] School of Mathematics and Statistics, Nanjing University of Information Science and Technology, Nanjing 210044, China
[4] Department of Mathematics, Faculty of Science, Khon Kaen University, Khon Kaen 40002, Thailand
* Correspondence: nkamsi@kku.ac.th

Abstract: In the last two decades, academicians have concentrated on the nanofluid squeezing flow between parallel plates. The increasing energy demands and their applications have seen the focus shifted to the hybrid nanofluid flows, but so much is still left to be investigated. This analysis is executed to explore the symmetry of the MHD squeezing nanofluid (MoS_2/H_2O) flow and the hybrid nanofluid (MoS_2–SiO_2/H_2O–$C_2H_6O_2$) flow between the parallel plates and their heat transport property. The heat transport phenomenon is analyzed with the magnetic field, thermal radiation, heat source/sink, suction/injection effect, and porous medium. In the present model, the plate situated above is in the movement towards the lower plate, and the latter is stretching with a linear velocity. The prevailing PDEs depicting the modeled problem with the aforementioned effects are transformed via similarity transformations and solved via the "bvp4c" function, which is an inbuilt function in MATLAB software. The control of the factors on the fields of velocity and temperature, heat transfer rate, velocity boundary layer patterns, and streamlines is investigated. The solution profiles are visually shown and explained. Furthermore, the Nusselt number at the bottom plate is larger for the (MoS_2–SiO_2/H_2O–$C_2H_6O_2$) hybrid nanofluid than for the (MoS_2/H_2O) nanofluid flow. In the presence of suction/injection, the streamlines appear to be denser. In addition, the magnetic field has a thinning consequence on the velocity boundary layer region. The results of this study apply to several thermal systems, engineering, and industrial processes, which utilize nanofluid and hybrid nanofluid for cooling and heating processes.

Keywords: mono nanofluid; hybrid nanofluid; parallel plate; Darcy porous medium; heat generation/absorption; thermal radiation

Citation: Yaseen, M.; Rawat, S.K.; Shafiq, A.; Kumar, M.; Nonlaopon, K. Analysis of Heat Transfer of Mono and Hybrid Nanofluid Flow between Two Parallel Plates in a Darcy Porous Medium with Thermal Radiation and Heat Generation/Absorption. *Symmetry* **2022**, *14*, 1943. https://doi.org/10.3390/sym14091943

Academic Editors: Toshio Tagawa, Sergei D. Odintsov and Mikhail Sheremet

Received: 25 July 2022
Accepted: 10 September 2022
Published: 19 September 2022

1. Introduction

A high-heat-transfer rate is desired in many applications, including dehumidifiers, heat exchangers, evaporators, and power stations. As a result, concerned researchers aim to develop a variety of models and methods to increase the heat-transmission rate. Integrating nanoparticles into conventional fluids is a cutting-edge method for meeting the requirement for high-heat-transfer rates. When nanoparticles of one or more kinds are disseminated into a working fluid, the outcome is a nanofluid. Depending on the usage and its applications, nanoparticles of various materials are used, such as metal, oxides of metals, carbon nanotubes, carbides, etc. Mono nanofluids are formed when only one variety of nanoparticles are injected into the working fluid (Choi [1]). Many researchers (Choi et al. [2]) have investigated the characteristics of amalgamated and

hybrid materials, but there is an urgent necessity to extend the investigation to reap the benefits of hybrid nanofluids. When two or more types of nanoparticles (e.g., MoS_2 and SiO_2) are dispersed in a base fluid (e.g., H_2O and $C_2H_6O_2$), it is called the hybrid nanofluid. The component materials' characteristics can be acquired while forming a hybrid nanofluid. When compared to individual nanoliquids, hybrid nanofluids have higher chemical stability, thermal conductivity, physical strength, mechanical resistance, and so on. Thermophysical and chemical features of hybrid nanomaterials are noteworthy, which are not seen in the individual components.

The hybrid nanomaterials are broadly categorized into three groups (see [3–5]):

1. Metal nanomaterials. Alumina/nickel (Al_2O_3/Ni), alumina/copper (Al_2O_3/Cu), alumina/chromium (Al_2O_3/Cr), alumina/iron (Al_2O_3/Fe), magnesia/iron (MgO/Fe), and magnesium/carbon nanotube (Mg/CNT).
2. Ceramic nanomaterials. Ferric oxide/carbon nanotubes (Fe_3O_4/CNT), nickel/silica (Ni/SiO_2), silica/alumina (SiO_2/Al_2O_3), alumina/titanium oxide (Al_2O_3/TiO_2), and silicon carbide/alumina (SiC/Al_2O_3).
3. Polymer nanomaterials. polyester/titanium oxide (TiO_2), polymer/hydroxides, and polymer/carbon nanotubes (CNT).

The rate of heat transmission is one of the characteristics that differentiate between the nanofluids having one and more nanoparticles. With the aforementioned applications of hybrid nanofluids, some scholars have lately studied the flows of hybrid nanofluids. Of late, Ullah et al. [6] studied the aspects of entropy generation on a flow of hybrid nanofluid (SWCNT-MWCNT/kerosene oil) past a stretching sheet. Yaseen et al. [7] surveyed the influence of suction/injection on the hybrid nanofluid flow past a moving surface. Ullah et al. [8] published a study in which they analyzed the influence of the Hall current and the Lorentz force on ZnO-Ni/water hybrid nanofluid over a transient stretching and rotating disk. Garia et al. [9] surveyed the flow of nanofluid with MoS_2 and SiO_2 nanoparticles past a wedge and a cone and inferred the role of time lag during the transport of heat. A theoretical analysis of the influence of suction, injection, heat generation, and magnetohydrodynamic effects on a Williamson hybrid nanofluid (i.e., (MoS4–Cu)/water) over a stretching cylinder was done by Kavya et al. [10]. Raju et al. [11] inspected the heat transport property of two types of ternary hybrid nanofluids in an expanding or contracting porous channel. They considered ternary hybrid nanofluids with two different combinations of nanoparticles, graphene, carbon nanotubes, and aluminium oxide; and copper, silver, and copper oxide. Upadhya et al. [12] studied the entropy generation of an incompressible, steady Casson, micropolar, and hybrid nanofluid over a curved stretching sheet. They considered the hybrid nanofluid with silica SiO_2 and aluminium oxide Al_2O_3 nanoparticles dispersed in water. They concluded that the micropolar fluid shows higher entropy generation compared to the Casson and hybrid nanofluid. Ullah et al. [13] investigated the thermal radiation and thermal slip parameter effects on the flow of hybrid nanoliquid past a stretchable rotating disk. They considered the hybrid nanoliquid with a combination of AA7072 and AA7075 nanoparticles and water.

Because of its uses in a variety of sectors, the squeezing flow induced by two parallel plates has grabbed the curiosity of many researchers in recent years. There are many applications but are not limited to the manufacturing and production fields, such as chocolate fillers, electric motors, hydraulic lifts, moving pistons, power transmission squeezed film, and polymer processing. In the aforementioned applications, the flow of fluid occurs when plates move towards or away from each other. Furthermore, the study of flow between the two parallel plates has received much importance due to their direct real-world applications in engineering sciences, such as viscometers, compression shaping, injection, the polymer and food industries, liquid-metal lubrication, and so on. Applications of squeezing problems can also be seen in tunnels of roads and railway lines, hydropower station caverns, water conveyance tunnels, underground sports halls, and oil and gas storage caverns. Singh et al. [14] surveyed the impact of velocity slip on the time-dependent flow of four different water-based nanofluids between two plates placed

parallel to each other. Salehi et al. [15] scrutinized the heat-transport property of squeezing MHD hybrid nanofluid flow induced by the two infinite plates placed parallel to each other. They inferred from their findings that as the squeeze number grows so does the thermal profile. The influence of the amalgamation of two different nanoparticles, Cu and Al_2O_3, in the flow with water as a working fluid in the middle of two parallel plates was scrutinized by Khashi'ie et al. [16]. They discussed their model with the assumption that the flow was induced due to the movement of the upper plate and the deformation of the lower plate. Kapen et al. [17] conducted an analysis to scrutinize the consequence of injection on hybrid nanofluid flow (Cu-Al_2O_3/water) between two stationary parallel plates and performed the stability analysis of their solution. The two-dimensional squeezing unsteady MHD Casson fluid flow between two parallel plates with nonlinear radiation was scrutinized by Kumar et al. [18]. Shah et al. [19] conducted an analysis to scrutinize the effect of the Hall current and electric field on a flow of nanofluid with micropolar nature between two parallel and rotating plates. Li et al. [20] studied the axisymmetric transient squeezing flow of the Newtonian non-conducting fluid between the two circular horizontal plates in a porous medium.

Heat generation/absorption and thermal radiation cannot be ignored at high-functioning temperatures. The awareness of the two aforementioned factors is a consideration in the design of appropriate tools since many technical activities occur at high temperatures. They also play an important part in many manufacturing units, such as glass manufacturing and construction of furnaces, and industrial-related applications, such as thrust systems in rockets, plasma mechanics, spaceships, nuclear plant ignition processes, solar radiations, and compressors of ships. The literature is rich in studies which deal with the effect of generation/absorption of heat or radiation. Ullah [21] analyzed the influence of heat source and thermal radiation on the flow of hybrid nanofluid. He considered the flow over the disk surface in a porous medium and hybrid nanofluid consisting of γ—ALOOH and AA7075 nanoparticles and gasoline oil as the working fluid. Henda et al. [22] looked upon the combined influence of radiation and heat sink/source on the third-grade bioconvective nanofluid flow induced by a stretched cylinder. Mishra and Kumar [23] analyzed the consequences of radiation on the heat-transmission performance of a nanofluid flow over a stretching sheet. Rawat and Kumar [24] published a study with an analysis of the heat-transference property of nanofluid flow with copper nanoparticles past a stretching surface under the combined impact of heat sink/source and thermal radiation. Ullah et al. [25] studied the combined influence of a thermal-heat source and the exponential space heart source on the heat-transport rate of a nanofluid on an infinite and rotating disk. Sharma et al. [26] inspected the influence of thermal radiation on the graphene Maxwell nanofluid flow over a linearly stretched sheet. Ge-Jile et al. [27] scrutinized the heat-transport property of a nanofluid flow past a vertical cone in the presence of thermal radiation. They considered the nanofluid consisting of water as a working fluid with ferrous nanoparticles. Raju et al. [28] studied the cross-diffusion effects on the Carreau fluid flow over a wedge filled with gyro tactic microorganisms under the influence of thermal radiation. Ullah et al. [29] explored the influence of temperature-dependent viscosity and exponential heat source on the flow of a nanoliquid in a rotating system.

The flow passing through a porous media has a critical advantage in the diverse environmental and manufacturing settings, including the design of boilers, geophysics, and reactors that involve convective flow. Many academicians have investigated the uses and impact of the porous media on fluid flow because of the aforementioned applications. Nandeppanavar et al. [30] surveyed the heat-transport property of the time-independent flow of the Casson nanofluid past a stretching sheet in the porous medium formulated by Darcy's law. Shah et al. [31] surveyed the rotational flow of micropolar nanofluid with CNT nanoparticles in the several base fluids between the horizontal and parallel plates in a porous medium formulated by Darcy–Forchheimer's law. Shafiq et al. [32] surveyed the nanofluid flow with thermal slip and convective heating in a rotating structure embedded in a porous medium characterized by the Darcy–Forchheimer relation. Ahmad et al. [33]

published a comparative study describing the heat-transport property of mono nanofluid (Cu/water) and hybrid nanofluid (Al_2O_3-Cu/water) flow through a stretching surface in a porous medium. Mishra and Kumar [34] studied the impact of a porous medium on the heat- and mass-transmission property of a nanofluid flow past a wedge. Yaseen et al. [35] published a comparative study describing the heat-transport property of hybrid nanofluid (MoS_2–SiO_2/kerosene oil) and (MoS_2/kerosene oil) nanofluid flow amid the two disks in a rotating state in a porous medium characterized by the Darcy–Forchheimer relation. Ullah et al. [36] investigated the significance of entropy generation in the flow of Ethylene glycol/water nanofluid in a rotating frame in a Darcy–Forchheimer porous medium. Hayat et al. [37] investigated the entropy optimization in the nonlinear mixed convective unsteady magnetohydrodynamic flow of nanomaterials in porous space. Li et al. [38] inspected the flow of MHD third-grade liquid through Darcy–Forchheimer's porous space with homogeneous–heterogeneous reactions. Ullah [39] performed the theoretical investigation of MHD nanofluid over a rotating and stretching disk in a Darcy–Forchheimer porous medium with zero-mass flux.

There has been a great amount of concern regarding the flow behavior and heat-transmission characteristics of nanofluid squeezing flow amid two parallel plates in recent years. The growing interest is because of the practical and theoretical values of squeezing flow. Squeezing flow has substantial applications in chocolate fillers, electric motors, hydraulic lifts, moving pistons, power transmission squeezed film, and polymer processing. The additional benefits are seen when the model is exposed to radiation, or the system has to deal with the generation of heat while in operation. Considering the aforementioned applications, the current paper deals with the squeezing flow model of hybrid nanofluid/nanofluid between the two parallel plates. The literature still lacks a study that compares the heat-transmission property of the hybrid nanofluid and nanofluid. In this paper, the authors have conducted a comparative analysis of the MoS_2/H_2O nanofluid flow and the MoS_2–SiO_2/H_2O–$C_2H_6O_2$ hybrid nanofluid flow between the two parallel plates. The novelty of the article is to comparatively study the heat-transport property of MoS_2/H_2O nanofluid flow and the MoS_2–SiO_2/H_2O–$C_2H_6O_2$ hybrid nanofluid flow in the middle of two parallel plates. Furthermore, as a novelty, the combined effects of the Darcy porous medium, heat absorption/generation, and radiation are considered at the same time to comparatively study the heat-transport property of the MoS_2/H_2O nanofluid flow and the MoS_2–SiO_2/H_2O–$C_2H_6O_2$ hybrid nanofluid.

The current paper also answers the succeeding questions:

- Importance of the hybrid nanofluid flow amid two parallel plates in a porous medium;
- Comparison of the flow behavior of MoS_2/H_2O nanofluid flow and the MoS_2–SiO_2/H_2O–$C_2H_6O_2$ hybrid nanofluid flow;
- Visualization of thermal behavior of flow when heat source/sink and thermal radiation is inevitable;
- The difference in heat-transfer rates of MoS_2/H_2O nanofluid flow and the MoS_2–SiO_2/H_2O–$C_2H_6O_2$ hybrid nanofluid flow at the lower and upper plates.

2. Mathematical Modeling

2.1. Model Development

In this article, a two-dimensional unsteady hybrid nanofluid/nanofluid squeezing flow in the middle of two infinite parallel plates in a Darcy porous medium with a magnetic field $B(t) = (1-\alpha t)^{-0.5}B_0$ is considered (Figure 1). In this model, the influence of thermal radiation and heat source/sink are also deliberated, and the buoyancy effect (gravitational force) is not taken into account. The upper plate and lower plate are placed at a distance, $y = h(t) = \sqrt{\frac{v_f(1-\alpha t)}{b}}$. Moreover, the upper plate has velocity, $V_h = \frac{dh(t)}{dt} = -\frac{\alpha}{2}\sqrt{\frac{v_f}{b(1-\alpha t)}}$ (squeezing of fluid), and it is moving towards the lower plate. Note that the steady-state case of the model is recovered when $\alpha = 0$. Furthermore,

the temperatures of the lower and upper plates are designated as T_1 and T_2, respectively. Furthermore, the current model deals with the fluid suction/injection, and $v_w = -\frac{V_0}{1-\alpha t}$ is the wall mass velocity; where $V_0 > 0$ for suction, $V_0 < 0$ for injection, and $V_0 = 0$ corresponds to an impermeable plate. In addition, the lower plate displaces with linear velocity, $u_w = \frac{bx}{1-\alpha t}$, where $t < \frac{1}{\alpha}$ and the lower plate is stretching/shrinking.

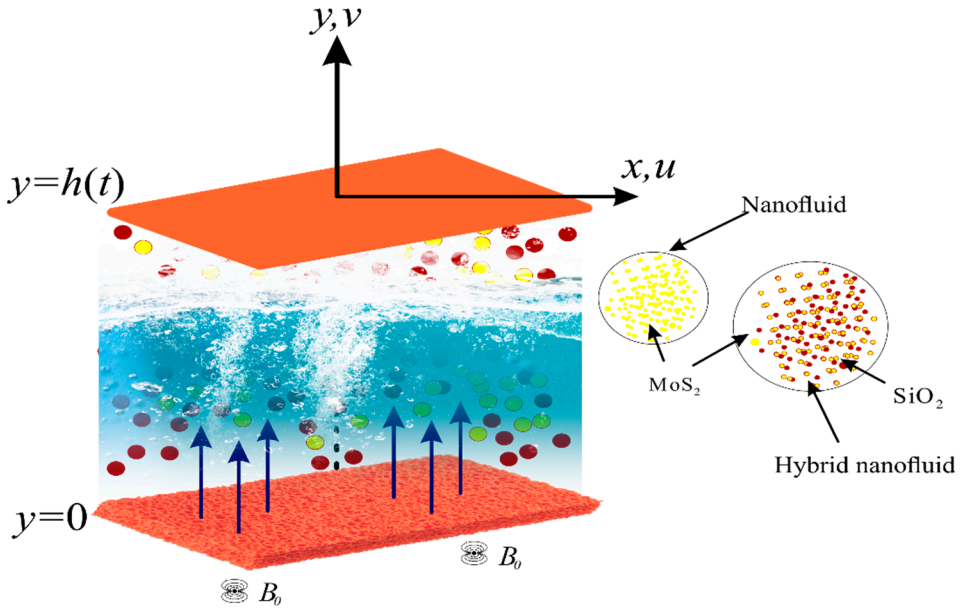

Figure 1. Physical model.

In view of the aforementioned assumptions, the governing equations are as follows (see Refs. [16,40]):

$$u_x + v_y = 0 \tag{1}$$

$$V_t + uV_x + vV_y = \frac{\mu_{hnf}}{\rho_{hnf}} V_{yy} - \frac{\sigma_{hnf}}{\rho_{hnf}} B(t)^2 V - \frac{\mu_{hnf}\phi^*}{\rho_{hnf} k_0} V \tag{2}$$

$$T_t + uT_x + vT_y = \frac{k_{hnf}}{(\rho C_p)_{hnf}} T_{yy} - \frac{1}{(\rho C_p)_{hnf}} (q_r)_y + \frac{Q_o}{(\rho C_p)_{hnf}} (T - T_0) \tag{3}$$

where $V = v_x - u_y$.

The current model considers the following boundary conditions:

$$\text{at Lower plate } (y = 0): \quad u = \lambda \frac{bx}{1-\alpha t}, \quad v = -\frac{V_0}{1-\alpha t}, \quad T = T_1 \tag{4}$$

$$\text{at Upper plate } (y = h(t)): \quad u = 0, \quad v = \frac{dh(t)}{dt}, \quad T = T_2 \tag{5}$$

In the aforementioned equation, (u, v) is the velocity in the (x, y) direction. Furthermore, the other symbol represents the following: T—temperature, ρ—density, μ—dynamic viscosity, C_p—heat capacity, k—thermal conductivity, $B(t)$—magnetic field strength, ϕ^* indicates porosity of the porous medium, k_o—permeability of the porous medium, λ is the stretching/shrinking parameter,Q_o—heat absorption/generation coefficient, and 'b' denotes the stretching/shrinking rate of the lower plate.

In the view of the Rosseland approximation, (q_r) is defined as (see Ref. [7]):

$$q_r = -\left(\frac{4\sigma^*}{3K^*_{hnf}}\right)\left(\frac{\partial T^4}{\partial y}\right) \tag{6}$$

where "σ^* stands for the Stefan–Boltzmann constant, and K^*_{hnf} stands for mean absorption coefficient".

Under the assumption that the variation of temperature is low between the layers, the following relationship is used (see Ref. [7]):

$$T^4 \cong \ 4\,T_2^3\,T - 3\,T_2^4 \tag{7}$$

With simple computations using the Equations (6) and (7), Equation (3) is simplified as:

$$(\rho C_p)_{hnf}(T_t + uT_x + vT_y) = \left(k_{hnf} + \frac{16}{3}\left(\frac{\sigma^* T_2^3}{k^*}\right)\right)\frac{\partial^2 T}{\partial y^2} + Q_o(T - T_0) \tag{8}$$

In this article, the two different fluid flows are analyzed, i.e., MoS_2/H_2O (nanofluid) flow and the MoS_2–SiO_2/H_2O–$C_2H_6O_2$ (hybrid nanofluid) flow. In the former fluid, the MoS_2 nanoparticles are individually disseminated in the water to prepare the mono-nanofluid (MoS_2/H_2O). In the latter case, initially MoS_2 nanoparticles and later SiO_2 nanoparticles are disseminated in the mixture, which is the combination of two fluids, water (H_2O) and ethylene glycol ($C_2H_6O_2$), to produce the hybrid nanofluid MoS_2–SiO_2/H_2O–$C_2H_6O_2$. The base fluid mixture in the hybrid nanofluid is taken as 50% water and 50% ethylene glycol. The mathematical correlations for the nanofluid and hybrid nanofluid properties and their properties are mentioned in Tables 1 and 2. For the evaluation of the thermophysical properties mentioned in Table 1, we adopt the correlations by Devi and Devi [41], which are feasible and correct based on the experimental validation. These correlations are built based on the physical assumptions. The subscripts are used as follows: "*f*—base fluid, *hnf* —hybrid nanofluid, and *nf*—nanofluid".

Table 1. Thermophysical properties of mono and hybrid nanofluid (see Devi and Devi [41]).

Properties	Nanofluid	Hybrid Nanofluid
Dynamic viscosity	$\frac{\mu_{nf}}{\mu_f} = (1-\varphi_1)^{-2.5}$	$\frac{\mu_{hnf}}{\mu_f} = (1-\varphi_1)^{-2.5}(1-\varphi_2)^{-2.5}.$
Density	$\rho_{nf} = \varphi_1\rho_{s1} + (1-\varphi_1)\rho_f$	$\rho_{hnf} = \varphi_2\rho_{s2} + (1-\varphi_2)\left[\varphi_1\rho_{s1} + (1-\varphi_1)\rho_f\right]$
Thermal conductivity	$\frac{k_{nf}}{k_f} = \left[\frac{k_{s1} + 2k_f - 2\varphi_1\left(k_f - k_{s1}\right)}{k_{s1} + 2k_f + \varphi_1\left(k_f - k_{s1}\right)}\right]$	$\frac{k_{hnf}}{k_{nf}} = \left[\frac{k_{s2} + 2k_{nf} - 2\varphi_2\left(k_{nf} - k_{s2}\right)}{k_{s2} + 2k_{nf} + \varphi_2\left(k_{nf} - k_{s2}\right)}\right]$ where $\frac{k_{nf}}{k_f} = \left[\frac{k_{s1} + 2k_f - 2\varphi_1\left(k_f - k_{s1}\right)}{k_{s1} + 2k_f + \varphi_1\left(k_f - k_{s1}\right)}\right]$
Electrical conductivity	$\frac{\sigma_{nf}}{\sigma_f} = 1 + \frac{3(\sigma-1)\varphi_1}{2+\sigma-(\sigma-1)\varphi_1}$ where $\sigma = \sigma_{s1}/\sigma_f$	$\frac{\sigma_{hnf}}{\sigma_{nf}} = \left[\frac{\sigma_{s2} + 2\sigma_{nf} - 2\varphi_2\left(\sigma_{nf} - \sigma_{s2}\right)}{\sigma_{s2} + 2\sigma_{nf} + \varphi_2\left(\sigma_{nf} - \sigma_{s2}\right)}\right]$ where $\frac{\sigma_{nf}}{\sigma_f} = \left[\frac{\sigma_{s1} + 2\sigma_f - 2\varphi_1\left(\sigma_f - \sigma_{s1}\right)}{\sigma_{s1} + 2\sigma_f + \varphi_1\left(\sigma_f - \sigma_{s1}\right)}\right]$
Heat capacitance	$(\rho C_p)_{nf} = \varphi_1(\rho C_p)_{s1} + (1-\varphi_1)(\rho C_p)_f$	$(\rho C_p)_{hnf} = \varphi_2(\rho C_p)_{s2} + (1-\varphi_2)\left[\varphi_1(\rho C_p)_{s1} + (1-\varphi_1)(\rho C_p)_f\right]$

Table 2. Properties of base fluid and nanoparticles (see [2,3]).

Properties/Constituents	H_2O	H_2O + EG (50:50)	MoS_2	SiO_2
C_p(J/kgK)	4179	3288	397.746	730
k(W/mK)	0.613	0.425	34.5	1.5
ρ(kg/m^3)	997.1	1056	5060	2650
$\sigma(\Omega m)^{-1}$	0.05	0.00509	2.09×10^4	1.0×10^{-18}
Pr	6.2	29.86		

2.2. Transforming the Governing Equations Using Similarity Transformation

The succeeding similarity variables are employed for transforming the equations described in Section 2.1 (see Ref. [16]):

$$\psi = \sqrt{\frac{bv_f}{1-\alpha t}} x f(\eta), \quad v = -\sqrt{\frac{bv_f}{1-\alpha t}} f(\eta), \quad u = \frac{bx}{1-\alpha t} f'(\eta), \quad \eta = \sqrt{\frac{b}{v_f(1-\alpha t)}} y, \quad \theta(\eta) = \frac{T-T_0}{T_2-T_0} \tag{9}$$

where T_0 is the reference temperature for hybrid nanofluid flow.

Using Equation (9), Equations (2), (4), and (8) are altered as:

$$\frac{1}{\zeta_1\zeta_2}(f'''') - \frac{Sq}{2}(\eta f''' + 3f'') - f'f'' + ff''' - \frac{\zeta_3}{\zeta_2} f'' M^2 - \frac{1}{\zeta_1\zeta_2}\frac{1}{Da} f'' = 0 \tag{10}$$

$$\frac{1}{Pr\zeta_4}\left(\zeta_5 + \frac{4}{3}R_d\right)\theta'' + \frac{1}{\zeta_4} Q\theta - \frac{Sq}{2}\eta\theta' + \theta' f = 0 \tag{11}$$

$$\begin{gathered} \theta(0) = \delta, \ \ f'(0) = \lambda, \ \ f(0) = S \\ f'(1) = 0, \ \ \theta(1) = 1, \ \ f(1) = \tfrac{Sq}{2} \end{gathered} \tag{12}$$

where $M^2\left(= \dfrac{\sigma_f {B_0}^2}{\rho_f\, b}\right)$ is the magnetic field parameter, $R_d\left(= \dfrac{4\sigma^* T_2^3}{k^* k_f}\right)$ stands for the thermal radiation parameter, $Da = \dfrac{k_0 b}{\phi^*(1-\alpha t) v_f}$ represents the Darcy number, $Sq = \dfrac{\alpha}{b}$ is the squeezing parameter, $Q = \dfrac{Q_0}{1-\alpha t}$ is the heat source/sink parameter, $Pr\left(= \frac{v_f}{\alpha_f}\right)$ stands for Prandtl number, $S\left(= \dfrac{V_0}{hb}\right)$ is the suction/injection parameter, and $\delta\left(= \dfrac{T_1 - T_0}{T_2 - T_0}\right)$ represents the temperature-ratio parameter. Furthermore, "$\lambda = 0$ implies the lower plate is static, $\lambda < 0$ implies shrinking, and $\lambda > 0$ implies the stretching of the lower plate". Moreover, $\zeta_1 = \dfrac{\mu_f}{\mu_{hnf}}$, $\zeta_2 = \dfrac{\rho_{hnf}}{\rho_f}$, $\zeta_3 = \dfrac{\sigma_{hnf}}{\sigma_f}$, $\zeta_4 = \dfrac{(\rho C_p)_{hnf}}{(\rho C_p)_f}$, $\zeta_5 = \dfrac{k_{hnf}}{k_f}$.

2.3. Nusselt Numbers

The Nusselt numbers that represent the heat transfer rates, (Nu_{x1}) and (Nu_{x2}) plates are defined as:

$$\text{at the lower plate : } Nu_{x1} = \frac{x(q_w + q_r)}{(T_2 - T_0)k_f}\bigg|_{y=0} \text{ and at the upper plate : } Nu_{x2} = \frac{x(q_w + q_r)}{(T_2 - T_0)k_f}\bigg|_{y=h(t)} \tag{13}$$

where $q_w + q_r$ is the heat flux in the presence of thermal radiation, which is defined as:

$$q_w + q_r = -\left(k_{hnf}\frac{\partial T}{\partial y} + \frac{4\sigma^*}{3k^*}\frac{\partial T^4}{\partial y}\right) \tag{14}$$

Substituting the values in Equation (13) from the Equations (9) and (14), the dimensionless forms of the Nusselt numbers are:

$$Nu^*_{x1} = (Re_x)^{-1/2} Nu_{x1} = -\left(\zeta_1 + \frac{4}{3}R_d\right)\theta'(0) \text{ (Lower plate)} \tag{15}$$

$$Nu^*_{x2} = (Re_x)^{-1/2} Nu_{x2} = -\left(\zeta_1 + \frac{4}{3}R_d\right)\theta'(1) \text{ (Upper plate)} \tag{16}$$

3. Numerical Method

The dimensionless Equations (10)–(12) are numerically solved utilizing "bvp4c solver" in the MATLAB software. The "bvp4c solver" is very efficient for the boundary value problems [42] and several researchers (see References [7,43]) have utilized it to analyze their flow models. The "bvp4c" solver is used through the following syntax:

"sol = bvp4c (@OdeBVP, @OdeBC, solinit, options)"

For solving, the following substitutions are made:

$$(y_1,\ y_2,\ y_3,\ y_4,\ y_5,\ y_6) = (f,\ f',\ f'',\ f''',\ \theta,\ \theta')$$

The MATLAB syntax written to solve the system is as follows:

$$\begin{pmatrix} yy_1 \\ yy_2 \end{pmatrix} = \begin{pmatrix} \zeta_1\zeta_2\left(\frac{Sq}{2}(3y_3 + \eta y_4) + y_2y_3 - y_1y_4 + \frac{\zeta_3}{\zeta_2}M^2y_3 + \frac{1}{\zeta_1\zeta_2}\frac{1}{Da}y_3\right); \\ \dfrac{-\frac{1}{\zeta_4}Q\,y_5 + \frac{Sq}{2}\eta y_6 - fy_6}{\frac{1}{Pr\zeta_4}\left(\zeta_5 + \frac{4}{3}R_d\right)}; \end{pmatrix} \tag{17}$$

and the initial conditions associated with the above system are as follows:

$$y_0(2) = \lambda,\ y_0(1) = S,\ y_0(5) = \delta,\ y_1(2) = 0,\ y_1(1) = \frac{Sq}{2},\ y_1(5) = 1 \tag{18}$$

Authors have utilized the aforementioned procedure to numerically solve the system represented by Equations (17) and (18). The missing values, $f''(1)$,$f''(0)$,$\theta'(1)$ and $\theta'(0)$", are required to initiate the procedure of finding the numerical solution. The step size to carry out the computations was set as 0.01 and $\eta = 1$. When the boundary conditions given in Equation (18) were fulfilled, the process of determining the numerical solution was terminated. Authors have validated the present results by presenting a comparison with the results of the published study of Hayat et al. [44] and Khashi'ie et al. [16] (see Table 3). A good agreement between the results is seen. Hence, this validates the results of this study.

Table 3. Comparison of values of $f''(1)$ and $f''(0)$ when $Sq = \varphi_1 = \varphi_2 = \frac{1}{Da} = Q = R_d = 0, \lambda = 1$ for various M.

		$f''(0)$			$f''(1)$		
M	***S***	**Khashi'ie et al. [16]**	**Hayat et al. [44]**	**Present**	**Khashi'ie et al. [16]**	**Hayat et al. [44]**	**Present**
0	0.5	−7.4111525	−7.411153	−7.41115256	4.7133028	4.713303	4.71330278
1	0.5	−7.5916177	−7.591618	−7.5916177	4.7390165	4.739017	4.7390165
4	0.5	−8.1103342	−8.110334	−8.11033423	4.8202511	4.820251	4.82025109
9	0.5	−8.9100956	−8.910096	−8.91009566	4.9648698	4.96487	4.9648698
4	0	−4.5878911	−4.587891	−4.5878911	1.8424469	1.842447	1.84244688
4	0.3	−6.6656620	−6.665662	−6.66566187	3.6536948	3.653695	3.65369492
4	0.6	−8.8514442	−8.851444	−8.85144422	5.3912475	5.391248	5.39124755
4	1	−11.9485843	−11.948584	−11.94858428	7.5934262	7.593426	7.59342617

4. Results and Discussion

This fragment analyzes the impact of pertinent flow parameters, such as "magnetic-field parameter, Darcy number, stretching/shrinking parameter, squeezing parameter, heat-generation/absorption parameter, injection/suction, and thermal-radiation parameter" on the velocity, $f'(\eta)$, temperature, $\theta(\eta)$, streamlines, and velocity boundary layer patterns. A comparative analysis of solution profiles for the nanofluid, MoS_2/H_2O, and hybrid nanofluid, MoS_2–SiO_2/H_2O–$C_2H_6O_2$, is presented in Figures 2–17. In the figures, "solid lines embody the solution for hybrid nanofluid (i.e., designated by *hnf*), and the dotted lines embody the solution for nanofluid (i.e., designated by *nf*)". For the computations of the results, the parameters were fixed as: $\varphi_1 = \varphi_2 = \delta = 0.1$, $\lambda = 2$, $R_d = \eta = 1$, $M = 2$, $Q = 0.3$, $S = 0.5$, $Sq = 3.2$, $Da = 0.04$, $Pr = 6.2$ (for mono nanofluid), and $Pr = 29.82$ (for hybrid nanofluid), and any discrepancy from the aforementioned values is mentioned at the suitable place in the figure or table.

4.1. Velocity Profile

This subsection has been prepared to examine the characteristics of involved parameters on the velocity distributions. Figures 2–8 display the deviation in fluid velocity for varied values of involved parameters. Figure 2 exhibits the behavior of velocity when the hybrid nanofluid/nanofluid flow between the parallel plates when the upper plate is moving. It is observed that velocity at/near the lower plate is affected by the stretching of the lower plate. Figure 3 displays the deviation in velocity for varied values of the magnetic parameter (M). Near the lower plate, the velocity falls with an increment in the value of the magnetic parameter. However, a transition point exists near $\eta \sim 0.5$. After this transition point, the velocity shows contrary behavior. The interface of a strong magnetic field represents remarkable decay of the flow of fluid. As M is assuming the high values, the Lorentz forces come into play, which reduces the liquid flow. The existence of a magnetic field challenges the flowing status and finally decelerates the radial velocity. Thus, magnetohydrodynamics is a procedure that controls fluid motion.

Figure 4 represents the alterations in the velocity as a function of the Darcy number (Da). Near the lower plate, velocity surges with an increment in the Darcy number. However, a transition point exists near $\eta \sim 0.5$. After this transition point, the velocity shows contrary behavior. Darcy number (Da) represents the "relative effect of the permeability of the medium versus its cross-sectional area", and permeability evaluates the surface capacity to flow fluid through its membrane. The increasing permeability near the lower plate restricts the motion of the fluid. As an outcome, when the Darcy number (Da) is increased, the velocity profiles fall near the upper plate due to more resistance to the flow.

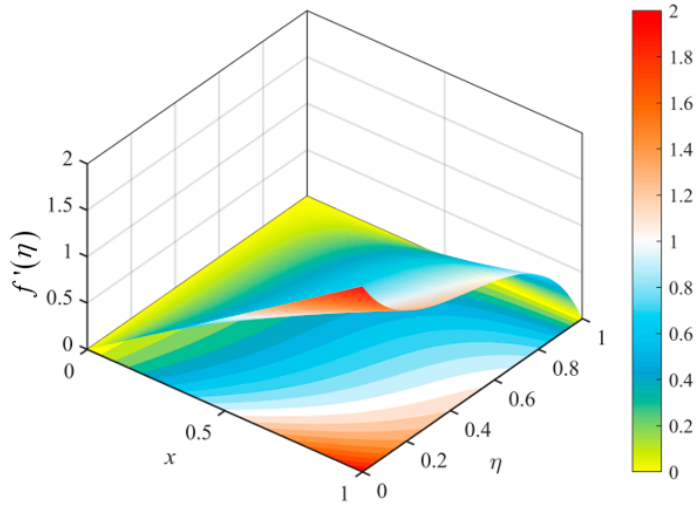

Figure 2. Behavior of velocity profile, $f'(\eta)$.

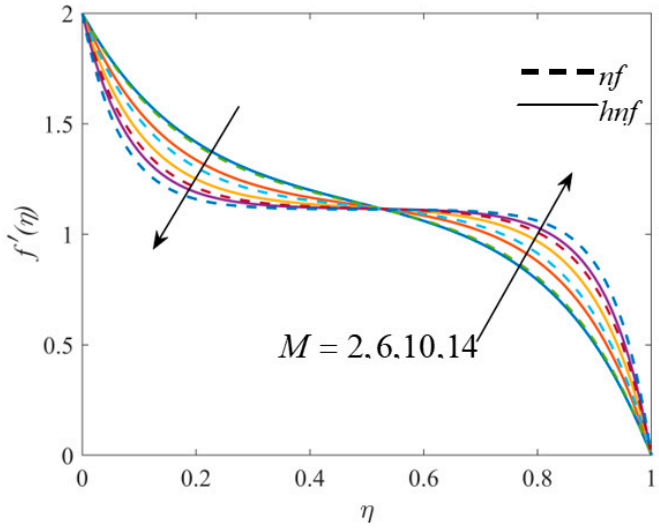

Figure 3. Behavior of velocity profile $f'(\eta)$, with M.

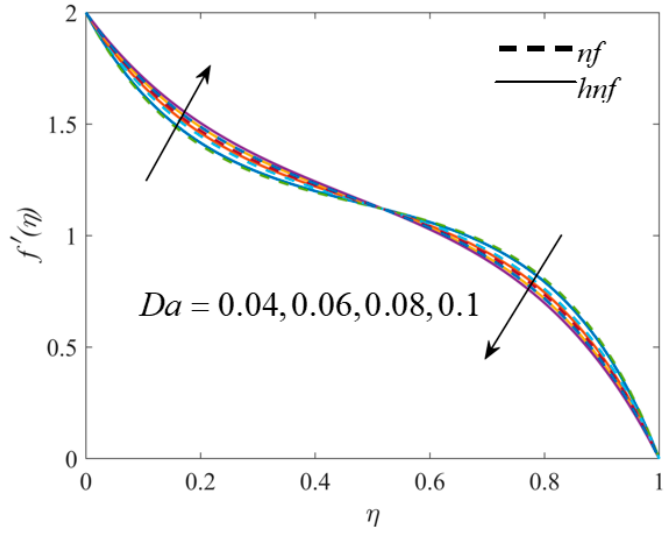

Figure 4. Behavior of velocity profile, $f'(\eta)$, with Da.

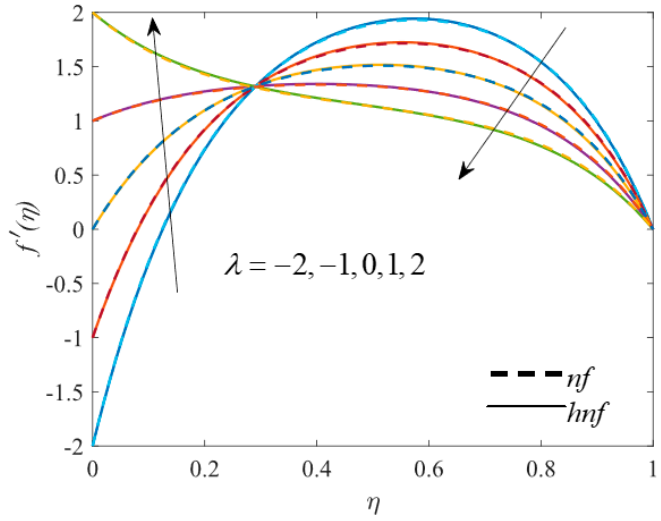

Figure 5. Behavior of velocity profile, $f'(\eta)$, with λ.

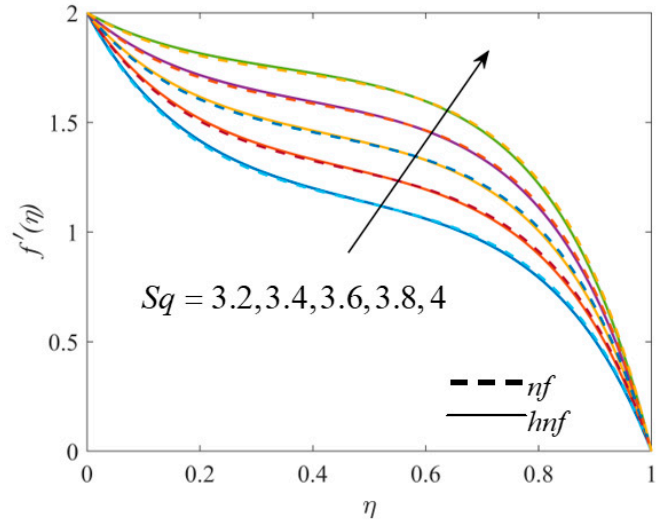

Figure 6. Behavior of velocity profile, $f'(\eta)$, with Sq.

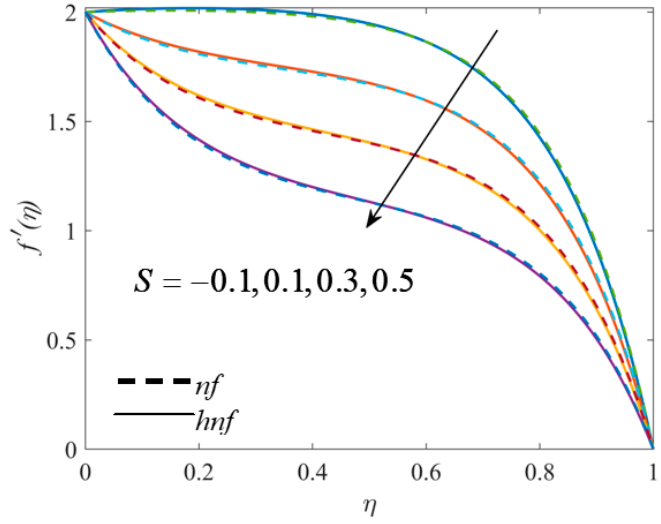

Figure 7. Behavior of velocity profile, $f'(\eta)$, with S.

Impressions of the shrinking/stretching parameter (λ) on the non-dimensional velocity are showcased in Figure 5. It is seen that the velocity, $f'(\eta)$, shows dual behavior with (λ). There exists a transition point near $\eta \sim 0.3$. The velocity, $f'(\eta)$, upsurges in the locality of the lower disk, but after the transition point, the velocity, $f'(\eta)$, decreases. This result indicates that the stretching of the lower plate enhances the velocity in the neighborhood of the lower plate. However, as the upper plate is in movement towards the direction of the lower plate, the behavior of the velocity with an increment in the parameter (λ) is reversed.

Figure 6 depicts the alterations in the velocity profile as a function of the squeezing parameter (*Sq*). The squeezing effect is instigated from the upper plate due to its movement towards the lower plate. It is seen that as the squeezing parameter (*Sq*) upsurges, the velocity of the fluid also increases. Figure 7 reveals the velocity profile with variation in the suction/injection parameter (*S*). The figure displays that the velocity rises with the application of injection in comparison to suction. Suction/injection is often used as a tool for avoiding the boundary layer separation, and in the present model, the increase in velocity is witnessed when the injection is applied, as seen in the figure. Hence, in the present model, the injection is more effective to defer the separation of the boundary layer.

In the Figures 2–7, velocity, $f'(\eta)$, is presented for MoS_2–SiO_2/H_2O–$C_2H_6O_2$ (hybrid nanofluid) and MoS_2/H_2O (nanofluid). It is observed that near the lower plate, MoS_2–SiO_2/H_2O–$C_2H_6O_2$ (hybrid nanofluid) has greater velocity, but after the transition point, a reverse pattern is witnessed, i.e., MoS_2/H_2O (nanofluid) has higher velocity near the upper plate.

4.2. Temperature Profile

This subsection has been prepared to examine the characteristics of the involved parameters on the temperature distributions. Figures 8–16 display the variation in temperature, $\theta(\eta)$, for diverse values of involved parameters. Figure 8 displays the deviation in temperature, $\theta(\eta)$, when the hybrid nanofluid/nanofluid flow between the parallel plates and when the upper plate is in movement. Figure 9 displays the deviation in temperature, $\theta(\eta)$, for diverse values of the magnetic parameter (*M*). It is perceived that the enhancement in the magnetic field decreases the temperature in both cases. The magnetic field instigates a Lorentz force that opposes the movement, which in opportunity gives a decrease in the thermal diffusion. The decreasing velocity near the lower plate is due to the application of a stronger magnetic field and causes the temperature to fall. Figure 10 represents the alterations in the temperature as a function of the Darcy number (*Da*). Darcy number (Da) represents the "relative effect of the permeability of the medium versus its cross-sectional area". The outcome implies that temperature rises with an upsurge in the Darcy number (*Da*). The flow experiences resistance while moving through the porous medium; hence, the temperature increases.

Impressions of the stretching/shrinking parameter (λ) on the temperature are showcased in Figure 11. In the present model, "$\lambda = 0$ implies the lower plate is static, $\lambda < 0$ implies shrinking, and $\lambda > 0$ implies the stretching of the lower plate". It is seen that the velocity, $f'(\eta)$, rises with the rising values of (λ). The results imply that the stretching of the lower plate enhances the temperature of the flow. Furthermore, as the extent of the shrinking of the lower plate increases, the temperature falls. Figure 12 exhibits the deviation in temperature, $\theta(\eta)$, for diverse values of the "volume fraction" (i.e., $\varphi = \varphi_1 = \varphi_2$). The plot directed that the rising value of volume-fraction parameters (i.e., $\varphi = \varphi_1 = \varphi_2$) raised the temperature. "Dispersion of supplementary nanoparticles supplements the capacity of hybrid nanofluid to transmit heat (i.e., thermal conductivity)". Thus, the temperature rises with the increasing value of φ.

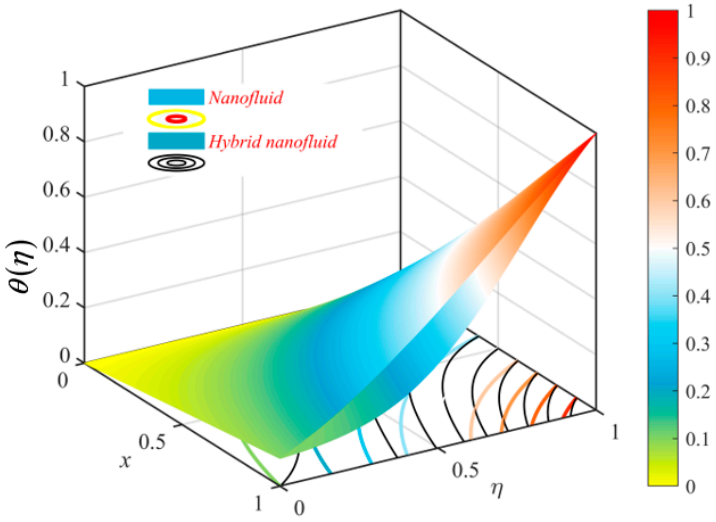

Figure 8. Behavior of temperature profile, $\theta(\eta)$.

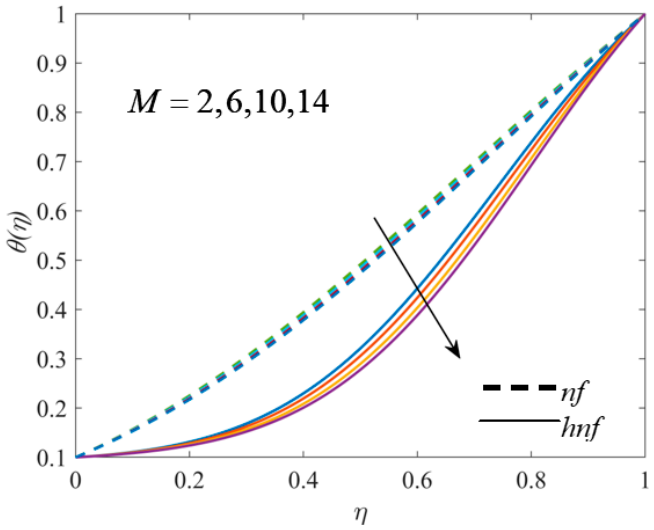

Figure 9. Behavior of temperature profile, $\theta(\eta)$, with M.

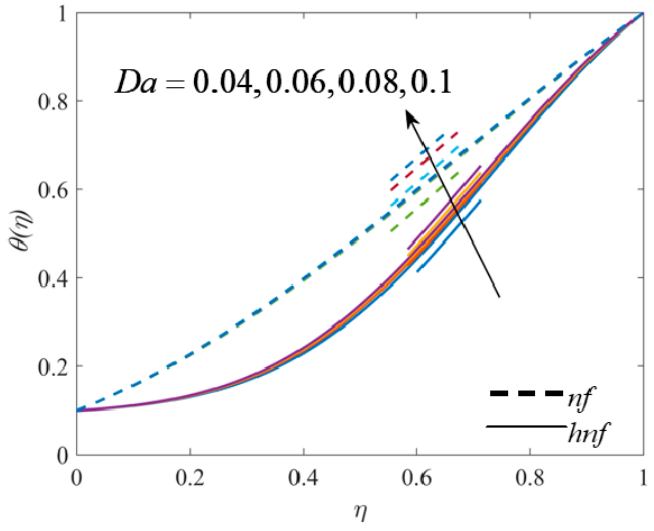

Figure 10. Behavior of temperature profile, $\theta(\eta)$, with Da.

Figure 13 depicts the alterations in the temperature with varying squeezing parameters (Sq). The figure clearly shows that when the parameter (Sq) is increased, the temperature decreases. This implies that the movement of the upper plate towards the lower plates restricts the thermal diffusion, and hence, the temperature decreases. Figure 14 reveals the inclining upshots of temperature when the "heat generation/absorption parameter" (Q) rises. The higher estimations of a parameter (Q) cause temperature to grow. The positive values of the parameter (Q) imply the generation of heat in the system, and increasing values correspond to more amounts of heat being generated. Hence, the temperature rises with higher estimations of the heat-generation parameter (Q). Figure 15 demonstrates the variation trend of non-dimensional temperature, $\theta(\eta)$, due to fluctuating values of the suction/injection parameter (S). The rise in $\theta(\eta)$ is observed when parameter S is increased. Temperature is found to be higher for the suction value in comparison to the injection value. Suction corresponds to sucking out the layers separated from the boundary layer. The fluid layers gain momentum with the implementation of suction, and hence, the temperature increases. Figure 16 displays the variation in the $\theta(\eta)$ for diverse values of the radiation parameter (R_d). It is witnessed that the $\theta(\eta)$ rises with the increment in the radiation parameter (R_d). An increase in thermal radiation leads to a decline in the coefficient of heat absorption, which elevates the fluid temperature. Thus, the increased quantity of heat transmitted in the area as a result of enhanced radiation raises the temperature $\theta(\eta)$.

In the aforementioned figures, the temperature, $\theta(\eta)$, is presented for MoS_2–SiO_2/H_2O–$C_2H_6O_2$ (hybrid nanofluid) and MoS_2/H_2O (nanofluid). It is observed that MoS_2/H_2O (nanofluid) flow has a higher temperature in comparison to the flow of MoS_2–SiO_2/H_2O–$C_2H_6O_2$ (hybrid nanofluid).

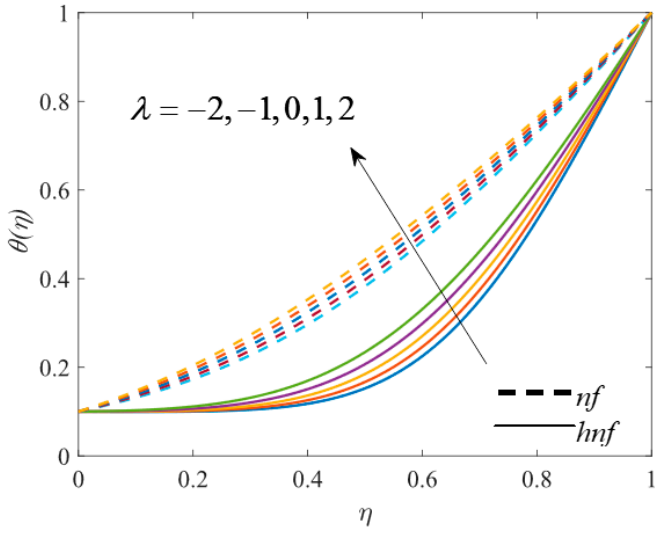

Figure 11. Behavior of temperature profile, $\theta(\eta)$, with λ.

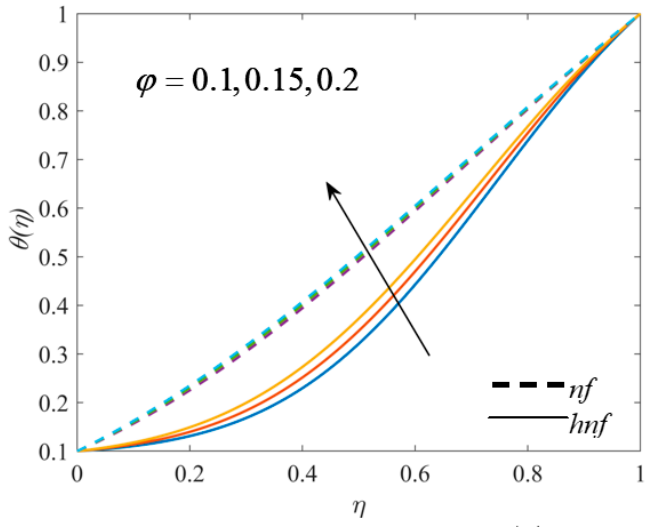

Figure 12. Behavior of temperature profile, $\theta(\eta)$, with φ.

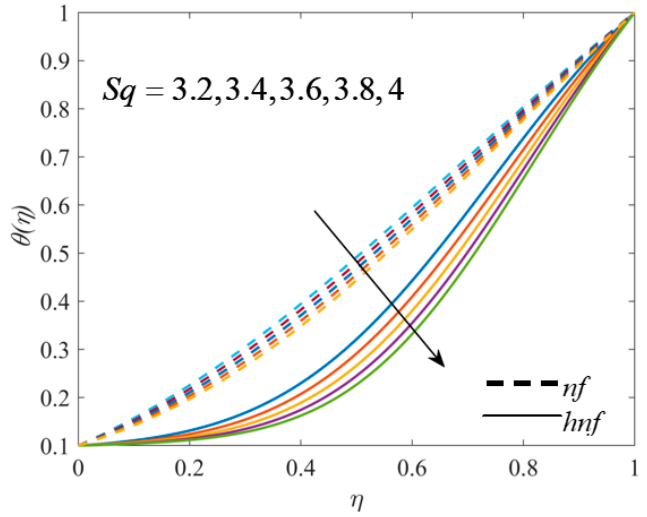

Figure 13. Behavior of temperature profile, $\theta(\eta)$, with Sq.

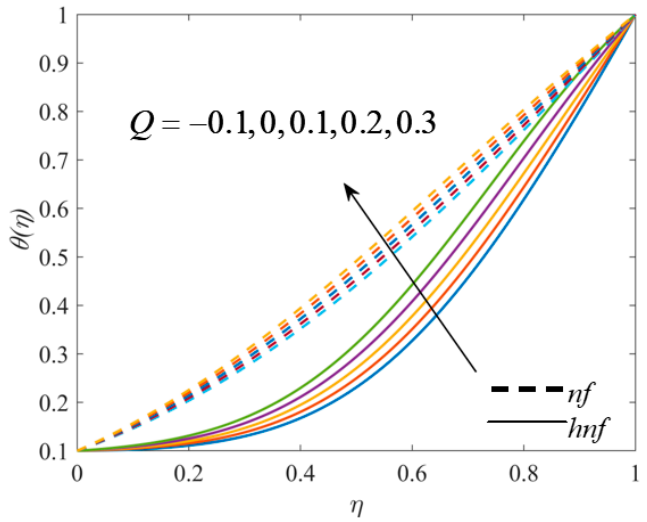

Figure 14. Behavior of temperature profile, $\theta(\eta)$, with Q.

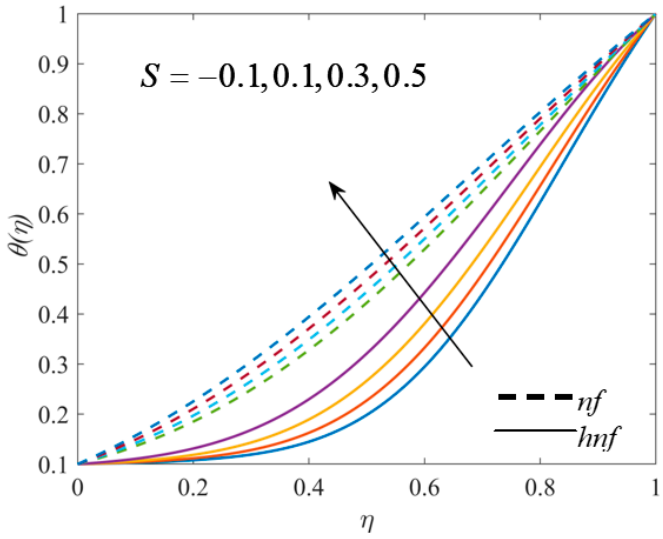

Figure 15. Behavior of temperature profile, $\theta(\eta)$, with S.

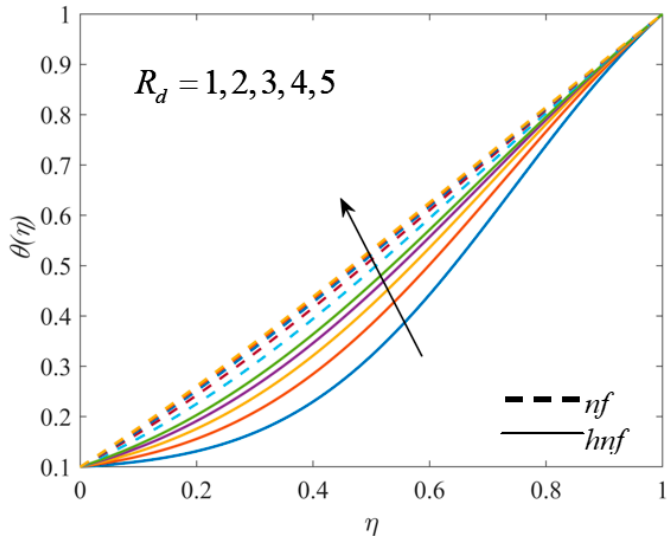

Figure 16. Behavior of temperature profile, $\theta(\eta)$, with R_d.

4.3. Streamlines and Velocity Boundary Layer Pattern

Figure 17 displays streamlines of the hybrid nanofluid flow with a different phase of suction/injection parameter. The streamlines are displayed when the flow is under the influence of injection ($S = -0.5$), suction ($S = 0.5$), and absence of both ($S = 0$). The streamlines depict the path of the particles suspended in the fluid and carried along with it. The tangent at any point in the streamline gives the direction of the fluid velocity at that point. It is clearly seen from Figure 17a,c that the streamlines become denser in the presence of suction or injection in comparison to the absence of both suction and injection ($S = 0$). These results further confirm the role of suction and injection in delaying the separation of the boundary layer during the flow.

Figure 18 displays the velocity boundary layer patterns when the flow is under the influence of a magnetic field ($M = 14$) and in the absence of a magnetic field ($M = 0$). From these aforementioned figures, we can do a comparatively analyze and visualize that the magnetic field has a thinning consequence on the velocity boundary layer region. The reason for this thinning consequence with the magnetic field is the generation of the Lorentz force due to the magnetic field, which opposes the movement of fluid.

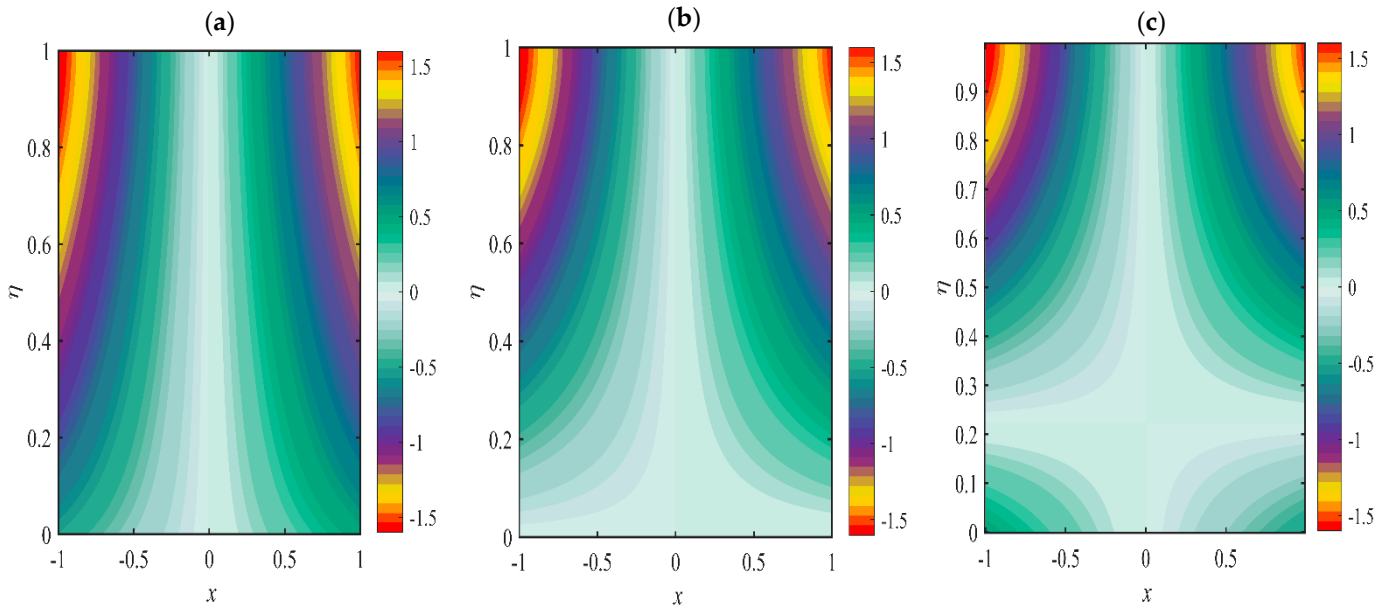

Figure 17. Streamline patterns for different values of suction/injection parameter (S). (**a**) $S = -0.5$; (**b**) $S = 0$; (**c**) $S = 0.5$.

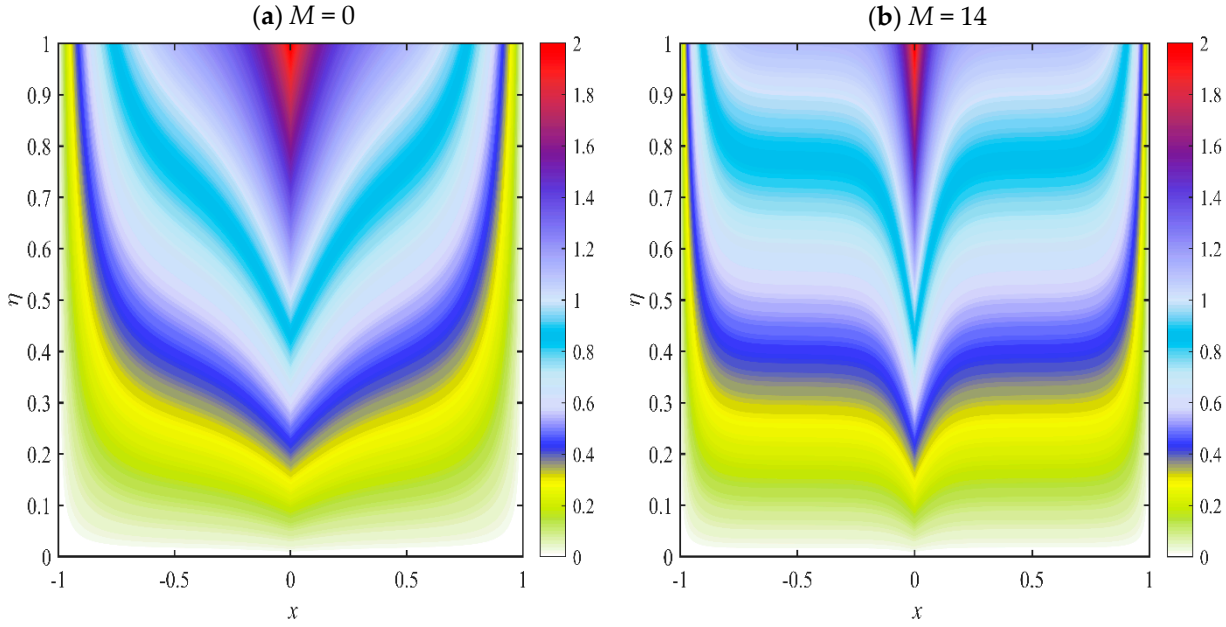

Figure 18. Velocity boundary layer pattern in the (**a**) absence of magnetic field and (**b**) presence of magnetic field.

4.4. Nusselt Numbers

Table 4 displays the behavior of the Nusselt numbers, Nu^*_{x1} and Nu^*_{x2}, at the lower and upper plate for different values of involved parameters. The Nusselt numbers represent the heat transference rates at the lower and upper plates. It is observed that the Darcy number (Da) has a positive correlation with the Nusselt number, Nu^*_{x2}, at the upper plate. However, contrary behavior is seen with the Nusselt number, Nu^*_{x1}, at the lower plate. Furthermore, the Nusselt number, Nu^*_{x1}, at the lower plate is positively correlated with the "magnetic parameter (M) and squeezing parameter (Sq)". However, contrary behavior is seen with the Nusselt number, Nu^*_{x2}, at the upper plate. In addition, the rising values of the "heat-generation/absorption parameter, stretching/shrinking parameter (λ), and

suction/injection parameter (S)" acts to enhance the Nusselt number, Nu^*_{x2}, at the upper plate. The rising values of "volume fraction" (φ_1, φ_2) and thermal radiation parameter (R_d) cause the Nusselt numbers at both the plates (Nu^*_{x1} and Nu^*_{x2}) to fall.

Table 4. Numerical values of heat-transfer coefficient of nanofluid (MoS_2/H_2O) and (MoS_2–SiO_2/H_2O–$C_2H_6O_2$) hybrid nanofluid.

									MoS_2/H_2O		$MoS_2-SiO_2/H_2O-C_2H_6O_2$	
Da	***M***	***Sq***	***λ***	***S***	φ_1	φ_2	***Q***	R_d	Nu^*_{x1}	Nu^*_{x2}	Nu^*_{x1}	Nu^*_{x2}
0.04	2	3.2	2	0.5	0.1	0.1	0.3	1	−1.34916991	−2.43760429	−0.21121505	−2.89742728
0.06									−1.36245421	−2.41385979	−0.21886821	−2.77005155
0.1									−1.37544707	−2.39085605	−0.22679853	−2.64453893
0.04	6								−1.31504548	−2.49970926	−0.19808463	−3.1328579
	14								−1.25838822	−2.60698691	−0.17464376	−3.62612217
	2	3.6							−1.13585234	−2.6143865	−0.12586435	−3.57622461
		4							−0.95338562	−2.7883278	−0.08616728	−4.15987165
		3.2	−2						−0.92386278	−2.96095613	−0.09282364	−4.81304915
			0						−1.12295604	−2.70537179	−0.12698724	−3.93950167
			2	−0.1					−0.79960932	−2.95380186	−0.06620933	−4.65301925
				0.3					−1.13661608	−2.61269763	−0.1260337	−3.56934147
				0.5	0.15	0.15			−1.52834388	−2.58065725	−0.3057826	−2.9868471
					0.2	0.2			−1.72972588	−2.74265991	−0.4340701	−3.0839793
					0.1	0.1	−0.1		−1.0896009	−3.22226056	−0.0312476	−5.69328936
							0.1		−1.21377331	−2.84089142	−0.11532536	−4.39973995
							0.3	3	−3.63080799	−4.81817893	−1.31211613	−5.20644542
								5	−5.99010125	−7.2109876	−3.064243	−7.52676646

In the present flow model, the Nusselt number at the lower plate is higher for MoS_2–SiO_2/H_2O–$C_2H_6O_2$ (hybrid nanofluid) flow in comparison to MoS_2/H_2O (nanofluid) flow. However, contrary behavior is seen at the upper plate.

5. Conclusions

This study investigates the "unsteady MHD two-dimensional squeezing flow of the MoS_2–SiO_2/H_2O–$C_2H_6O_2$ (hybrid nanofluid) and MoS_2/H_2O (nanofluid) between two parallel plates". Modeling of the flow is done with the assumptions of "heat-generation/absorption effect, porous medium, radiation, and injection/suction effect". The principal equations are handled by the "bvp4c" function of the MATLAB software.

Some vital conclusions of the present analysis are:

- The injection effect and the shrinking of the lower plate aid the hybrid nanofluid flow.
- The thermal radiation parameter and heat sink/source parameter have a positive correlation with the thermal field.
- The hybrid nanofluid flow has a higher Nusselt number at the lower plate than the nanofluid.
- The streamlines become denser under the influence of suction and injection effects.
- The presence of a magnetic field has a thinning consequence on the velocity boundary layer region.
- The results of this study apply to several thermal systems, engineering, and industrial processes, which utilize nanofluid and hybrid nanofluid for cooling and heating processes.

Derivation of the Flow Problem in Appendix A.

Author Contributions: Conceptualization, M.Y., S.K.R., A.S., M.K. and K.N.; Investigation, M.Y., S.K.R., A.S., M.K. and K.N.; Writing—original draft preparation, M.Y. and S.K.R.; Writing—review and editing, A.S., M.K. and K.N. All authors have read and agreed to the published version of the manuscript.

Funding: This research received no external funding.

Data Availability Statement: Not Applicable.

Conflicts of Interest: The authors declare no conflict of interest.

Nomenclature

Roman Letters			
b	constant	v_w	Velocity of mass flux (m/s)
B_o	Magnetic induction (W/m^2)	(x, y)	Cartesian coordinates (m)
$B(t)$	Magnetic field (kg/(s^2·m^2))		
Da	Darcy number	***Greek symbols***	
$f'(\eta)$	Dimensionless velocity	α	Constant
$h(t)$	Distance between plates (m)	λ	Stretching/shrinking parameter
k	Thermal conductivity (W/mK)	δ	Temperature-ratio parameter
K^*	Mean absorption coefficient (m^{-1})	ϕ^*	Porosity of the porous medium
k_o	Permeability of the porous medium (m^2)	φ_1	Solid volume fraction of MoS_2
M	Magnetic-field parameter	φ_2	Solid volume fraction of SiO_2
Nu_x^*	Nusselt number	ν	Kinematic viscosity (m^2/s)
Pr	Prandtl number	μ	Dynamic viscosity (kg m^{-1} s^{-1})
Q	Heat-source/sink parameter	ρ	Density (kg/m^3)
q_r	Radiative-heat flux (W/m^2)	ψ	Stream function
R_d	Radiation parameter	σ^*	Stefan–Boltzmann constant (W. m^{-2}. K^{-4})
$\mathrm{Re_x}$	Local Reynolds number	σ	Electrical conductivity ((s^3. m^2)/kg)
Sq	Squeezing parameter	ρC_p	Heat capacity (J/m^{3}K)
S	Suction/injection parameter	η	Similarity variable
t	Time (s)	$\zeta_i (i = 1-5)$	Constant
T	Temperature (K)		
T_o	Reference temperature (K)	***Subscripts***	
T_1	Lower plate temperature (K)		
T_2	Upper plate temperature (K)	f	Base fluid
θ	Dimensionless temperature	nf	Nanofluid
(u, v)	Components of velocity (m/s)	hnf	Hybrid nanofluid
u_w	Stretching velocity (m/s)		
V_o	Constant	***Superscripts***	
V_h	Velocity of the upper plate moving towards/away from the lower plate (m/s)	$'$	Derivative w. r. to η

Appendix A. Derivation of the Flow Problem

The flow problem has the following governing equations and boundary conditions:
Continuity equation:

$$u_x + v_y = 0 \tag{A1}$$

Momentum equation:

$$V_t + uV_x + vV_y = \frac{\mu_{hnf}}{\rho_{hnf}} V_{yy} - \frac{\sigma_{hnf}}{\rho_{hnf}} B(t)^2 V - \frac{\mu_{hnf}\phi^*}{\rho_{hnf} k_0} V \tag{A2}$$

where $V = v_x - u_y$.

Energy equation:

$$\left(\rho C_p\right)_{hnf} \left(T_t + uT_x + vT_y\right) = \left(k_{hnf} + \frac{16}{3}\left(\frac{\sigma^* T_\infty^3}{k^*}\right)\right)\frac{\partial^2 T}{\partial y^2} + Q_o(T - T_0) \tag{A3}$$

Boundary condition:

$$\begin{aligned} \text{at Lower plate } (y = 0): \quad u = \lambda \frac{bx}{1 - \alpha t}, \quad v = -\frac{V_0}{1 - \alpha t}, \quad T = T_1 \\ \text{at Upper plate } (y = h(t)): \quad u = 0, \quad v = \frac{dh(t)}{dt}, \quad T = T_2 \end{aligned} \tag{A4}$$

The dimensionless variables are given as

$$\psi = \sqrt{\frac{bv_f}{1-\alpha t}} x f(\eta),\ v = -\sqrt{\frac{bv_f}{1-\alpha t}} f(\eta),\ u = \frac{bx}{1-\alpha t} f'(\eta),\ \eta = \sqrt{\frac{b}{v_f(1-\alpha t)}} y,\ \theta(\eta) = \frac{T-T_0}{T_2-T_0} \tag{A5}$$

From $u = \dfrac{bx}{1-\alpha t} f'(\eta)$ and $v = -\sqrt{\dfrac{bv_f}{1-\alpha t}} f(\eta)$, we get

$$\begin{gathered} V = -\left(\sqrt{\frac{b}{v_f}} \frac{bx}{(1-\alpha t)^{3/2}}\right) f'',\ V_t = -\left(\sqrt{\frac{b}{v_f}} \frac{\alpha bx}{2(1-\alpha t)^{5/2}}\right) \{3f'' + \eta f'''\} \\ V_x = -\left(\sqrt{\frac{b}{v_f}} \frac{b}{(1-\alpha t)^{3/2}}\right) f'',\ V_y = -\left(\frac{b^2 x}{v_f(1-\alpha t)^2}\right) f''',\ V_{yy} = -\left(\sqrt{\frac{b}{v_f}} \frac{b^2 x}{v_f(1-\alpha t)^{5/2}}\right) f'''', \end{gathered} \tag{A6}$$

From $\theta(\eta) = \dfrac{T-T_0}{T_2-T_0}$, we get

$$\begin{gathered} T_t = (T_2-T_0)\eta\left(\frac{\alpha}{2(1-\alpha t)}\right)\theta',\ T_y = (T_2-T_0)\sqrt{\frac{b}{v_f(1-\alpha t)}}\theta' \\ T_{yy} = (T_2-T_0)\left(\frac{b}{v_f(1-\alpha t)}\right)\theta'',\ T_x = 0 \end{gathered} \tag{A7}$$

Appendix A.1. Derivation of Continuity Equation

Substitute (A5) into Equation (A1) to obtain

$$\begin{aligned} u_x + v_y &= \frac{b}{1-\alpha t} f'(\eta) - \frac{b}{1-\alpha t} f'(\eta) \\ &= 0 \end{aligned}$$

Thus, it satisfies the continuity equation.

Appendix A.2. Derivation of Momentum Equations

Substitute (A5) and (A6) into the Equation (A2) to obtain

$$\begin{gathered} V_t + uV_x + vV_y = \frac{\mu_{hnf}}{\rho_{hnf}} V_{yy} - \frac{\sigma_{hnf}}{\rho_{hnf}} B(t)^2 V - \frac{\mu_{hnf}\phi^*}{\rho_{hnf} k_0} V \\ -\left(\sqrt{\frac{b}{v_f}} \frac{b^2 x}{2(1-\alpha t)^{5/2}}\right)\left(\frac{\alpha}{b}\right)\{3f'' + \eta f'''\} + \left(-\left(\sqrt{\frac{b}{v_f}} \frac{b^2 x}{(1-\alpha t)^{5/2}}\right) f' f''\right) + \left(\sqrt{\frac{b}{v_f}} \frac{b^2 x}{(1-\alpha t)^{5/2}}\right) f f''' \\ = \frac{\mu_{hnf}}{v_f \rho_{hnf}}\left(-\left(\sqrt{\frac{b}{v_f}} \frac{b^2 x}{(1-\alpha t)^{5/2}}\right) f''''(\eta)\right) - \frac{\sigma_{hnf}}{\rho_{hnf}} \frac{B_0^2}{1-\alpha t}\left(-\left(\sqrt{\frac{b}{v_f}} \frac{bx}{(1-\alpha t)^{3/2}}\right) f''(\eta)\right) - \frac{\mu_{hnf}\phi^*}{\rho_{hnf} k_0}\left(-\left(\sqrt{\frac{b}{v_f}} \frac{bx}{(1-\alpha t)^{3/2}}\right) f''(\eta)\right) \end{gathered}$$

Divide both sides by $\left(\sqrt{\dfrac{b}{v_f}} \dfrac{b^2 x}{(1-\alpha t)^{5/2}}\right)$, we get

$$\frac{1}{\zeta_1 \zeta_2}\left(f''''\right) - \frac{Sq}{2}(\eta f''' + 3f'') - f' f'' + f f''' - \frac{\zeta_3}{\zeta_2} f'' M^2 - \frac{1}{\zeta_1 \zeta_2} \frac{1}{Da} f'' = 0 \tag{A8}$$

Appendix A.3. Derivation of Energy Equation

The energy equation is given by Equation (A3). Substitute (A5)–(A7) into Equation (A3) to get

$$(\rho C_p)_{hnf}(T_t + uT_x + vT_y) = \left(k_{hnf} + \frac{16}{3}\left(\frac{\sigma^* T_\infty^3}{k^*}\right)\right)\frac{\partial^2 T}{\partial y^2} + Q_o(T - T_0)$$

$$(T_2 - T_0)\eta\left(\frac{\alpha}{2(1-\alpha t)}\right)\theta' + u \times 0 - \sqrt{\frac{bv_f}{1-\alpha t}}f(T_2 - T_0)\sqrt{\frac{b}{v_f(1-\alpha t)}}\theta'$$

$$= \frac{k_f}{(\rho C_p)_{hnf}}\left(\frac{k_{hnf}}{k_f} + \frac{16}{3}\left(\frac{\sigma^* T_\infty^3}{k_f k^*}\right)\right)\left((T_2 - T_0)\left(\frac{b}{v_f(1-\alpha t)}\right)\theta''\right) + \frac{\sigma_{hnf}}{(\rho C_p)_{hnf}}\frac{{B_0}^2}{1-\alpha t}{u_w}^2 f{\prime}^2$$

Divide both sides by $(T_2 - T_0)\left(\frac{b}{(1-\alpha t)}\right)$, we get

$$\frac{1}{Pr\zeta_4}\left(\zeta_5 + \frac{4}{3}R_d\right)\theta'' + \frac{1}{\zeta_4}Q_0^*\theta - \frac{Sq}{2}\eta\theta' + \theta' f = 0 \tag{A9}$$

Appendix A.4. Derivation of Boundary Conditions

From (A4), we can see that when $y = 0$, then $\eta = 0$ and when $y = h(t)$, then $\eta = 1$. The derivation for boundary conditions at $\eta = 0$ and $\eta = 1$ is as follows:

From, $u = \lambda\frac{bx}{1-\alpha t}$, $u = 0$ and $u = \frac{bx}{1-\alpha t}f'(\eta)$, we have

$$\frac{bx}{1-\alpha t}f'(\eta) = \lambda\frac{bx}{1-\alpha t}$$

$$f'(\eta) = \lambda \qquad \text{at } \eta = 0$$

$$f'(\eta) = 0 \qquad \text{at } \eta = 1$$

From $v = -\frac{V_0}{1-\alpha t}$, $v = \frac{dh(t)}{dt}$ and $v = -\sqrt{\frac{bv_f}{1-\alpha t}}f(\eta)$, we have

$$-\sqrt{\frac{bv_f}{1-\alpha t}}f(\eta) = -\frac{V_0}{1-\alpha t}$$

$$f(\eta) = \frac{V_0}{hb}$$

$$f(\eta) = S \qquad \text{at } \eta = 0$$

$$-\sqrt{\frac{bv_f}{1-\alpha t}}f(\eta) = -\frac{\alpha}{2}\sqrt{\frac{v_f}{b(1-\alpha t)}}$$

$$f(\eta) = \frac{Sq}{2} \qquad \text{at } \eta = 1$$

From $T = T_1$, $T = T_2$ and $\theta(\eta) = \frac{T - T_0}{T_2 - T_0}$, we have

$$\theta(\eta) = \frac{T_1 - T_0}{T_2 - T_0}$$

$$\theta(\eta) = \delta \qquad \text{at } \eta = 0$$

$$\theta(\eta) = 1 \qquad \text{at } \eta = 1$$

where, $M^2 = \frac{\sigma_f {B_0}^2}{\rho_f\, b}$, $R_d = \frac{4\sigma^* T_\infty^3}{k^* k_f}$, $Da = \frac{k_0 b}{\phi^*(1-\alpha t)v_f}$, $Sq = \frac{\alpha}{b}$, $Q_0^* = \frac{Q_0}{1-\alpha t}$, $Pr\left(=\frac{v_f}{\alpha_f}\right)$, $S\left(=\frac{V_0}{hb}\right)$, $\delta\left(=\frac{T_1-T_0}{T_2-T_0}\right)$, $\zeta_1 = \frac{\mu_f}{\mu_{hnf}}$, $\zeta_2 = \frac{\rho_{hnf}}{\rho_f}$, $\zeta_3 = \frac{\sigma_{hnf}}{\sigma_f}$, $\zeta_4 = \frac{(\rho C_p)_{hnf}}{(\rho C_p)_f}$ and $\zeta_5 = \frac{k_{hnf}}{k_f}$ are constants.

References

1. Choi, S.U.S. Enhancing Thermal Conductivity of Fluids with Nanoparticles. *Am. Soc. Mech. Eng. Fluids Eng. Div.* **1995**, *231*, 99–105.
2. Choi, C.; Yoo, H.S.; Oh, J.M. Preparation and Heat Transfer Properties of Nanoparticle-in-Transformer Oil Dispersions as Advanced Energy-Efficient Coolants. *Curr. Appl. Phys.* **2008**, *8*, 710–712. [CrossRef]
3. Taylor-Pashow, K.M.L.; Della Rocca, J.; Huxford, R.C.; Lin, W. Hybrid Nanomaterials for Biomedical Applications. *Chem. Commun.* **2010**, *46*, 5832–5849. [CrossRef] [PubMed]
4. Masteri-Farahani, M.; Movassagh, J.; Taghavi, F.; Eghbali, P.; Salimi, F. Magnetite–Polyoxometalate Hybrid Nanomaterials: Synthesis and Characterization. *Chem. Eng. J.* **2012**, *184*, 342–346. [CrossRef]
5. Mehryan, S.A.M.; Izadpanahi, E.; Ghalambaz, M.; Chamkha, A.J. Mixed Convection Flow Caused by an Oscillating Cylinder in a Square Cavity Filled with Cu–Al_2O_3/Water Hybrid Nanofluid. *J. Therm. Anal. Calorim.* **2019**, *137*, 965–982. [CrossRef]
6. Ullah, I.; Hayat, T.; Alsaedi, A. Optimization of Entropy Production in Flow of Hybrid Nanomaterials through Darcy–Forchheimer Porous Space. *J. Therm. Anal. Calorim.* **2021**, *147*, 5855–5864. [CrossRef]
7. Yaseen, M.; Kumar, M.; Rawat, S.K. Assisting and Opposing Flow of a MHD Hybrid Nanofluid Flow Past a Permeable Moving Surface with Heat Source/Sink and Thermal Radiation. *Partial Differ. Equations Appl. Math.* **2021**, *4*, 100168. [CrossRef]
8. Ullah, I.; Jan, R.U.; Khan, H.; Alam, M.M. Improving the Thermal Performance of (ZnO-Ni/H_2O) Hybrid Nanofluid Flow over a Rotating System: The Applications of Darcy Forchheimer Theory. *Waves Random Complex Media* **2022**, 1–17. [CrossRef]
9. Garia, R.; Rawat, S.K.; Kumar, M.; Yaseen, M. Hybrid Nanofluid Flow over Two Different Geometries with Cattaneo-Christov Heat Flux Model and Heat Generation: A Model with Correlation Coefficient and Probable Error. *Chin. J. Phys.* **2021**, *74*, 421–439. [CrossRef]
10. Kavya, S.; Nagendramma, V.; Ahammad, N.A.; Ahmad, S.; Raju, C.S.K.; Shah, N.A. Magnetic-Hybrid Nanoparticles with Stretching/Shrinking Cylinder in a Suspension of MoS_4 and Copper Nanoparticles. *Int. Commun. Heat Mass Transf.* **2022**, *136*, 106150. [CrossRef]
11. Raju, C.S.K.; Ahammad, N.A.; Sajjan, K.; Shah, N.A.; Yook, S.J.; Kumar, M.D. Nonlinear Movements of Axisymmetric Ternary Hybrid Nanofluids in a Thermally Radiated Expanding or Contracting Permeable Darcy Walls with Different Shapes and Densities: Simple Linear Regression. *Int. Commun. Heat Mass Transf.* **2022**, *135*, 106110. [CrossRef]
12. Upadhya, S.M.; Raju, S.V.S.R.; Raju, C.S.K.; Shah, N.A.; Chung, J.D. Importance of Entropy Generation on Casson, Micropolar and Hybrid Magneto-Nanofluids in a Suspension of Cross Diffusion. *Chin. J. Phys.* **2022**, *77*, 1080–1101. [CrossRef]
13. Ullah, I.; Hayat, T.; Alsaedi, A.; Asghar, S. Dissipative Flow of Hybrid Nanoliquid (H_2O-Aluminum Alloy Nanoparticles) with Thermal Radiation. *Phys. Scr.* **2019**, *94*, 125708. [CrossRef]
14. Singh, K.; Rawat, S.K.; Kumar, M. Heat and Mass Transfer on Squeezing Unsteady MHD Nanofluid Flow between Parallel Plates with Slip Velocity Effect. *J. Nanosci.* **2016**, *2016*, 9708562. [CrossRef]
15. Salehi, S.; Nori, A.; Hosseinzadeh, K.; Ganji, D.D. Hydrothermal Analysis of MHD Squeezing Mixture Fluid Suspended by Hybrid Nanoparticles between Two Parallel Plates. *Case Stud. Therm. Eng.* **2020**, *21*, 100650. [CrossRef]
16. Khashi'ie, N.S.; Waini, I.; Arifin, N.M.; Pop, I. Unsteady Squeezing Flow of Cu-Al_2O_3/Water Hybrid Nanofluid in a Horizontal Channel with Magnetic Field. *Sci. Rep.* **2021**, *11*, 14128. [CrossRef]
17. Tiam Kapen, P.; Gervais Njingang Ketchate, C.; Fokwa, D.; Tchuen, G. Linear Stability Analysis of (Cu-Al_2O_3)/Water Hybrid Nanofluid Flow in Porous Media in Presence of Hydromagnetic, Small Suction and Injection Effects. *Alexandria Eng. J.* **2021**, *60*, 1525–1536. [CrossRef]
18. Sathish Kumar, M.; Sandeep, N.; Rushi Kumar, B.; Saleem, S. Effect of Aligned Magnetic Field on MHD Squeezing Flow of Casson Fluid between Parallel Plates. *Defect Diffus. Forum* **2018**, *384*, 1–11. [CrossRef]
19. Shah, Z.; Islam, S.; Gul, T.; Bonyah, E.; Altaf Khan, M. The Electrical MHD and Hall Current Impact on Micropolar Nanofluid Flow between Rotating Parallel Plates. *Results Phys.* **2018**, *9*, 1201–1214. [CrossRef]
20. Li, Y.M.; Ullah, I.; Ameer Ahammad, N.; Ullah, I.; Muhammad, T.; Asiri, S.A. Approximation of Unsteady Squeezing Flow through Porous Space with Slip Effect: DJM Approach. *Waves Random Complex Media* 2022. [CrossRef]
21. Ullah, I. Heat Transfer Enhancement in Marangoni Convection and Nonlinear Radiative Flow of Gasoline Oil Conveying Boehmite Alumina and Aluminum Alloy Nanoparticles. *Int. Commun. Heat Mass Transf.* **2022**, *132*, 105920. [CrossRef]
22. Ben Henda, M.; Waqas, H.; Hussain, M.; Khan, S.U.; Chammam, W.; Khan, S.A.; Tlili, I. Applications of Activation Energy along with Thermal and Exponential Space-Based Heat Source in Bioconvection Assessment of Magnetized Third Grade Nanofluid over Stretched Cylinder/Sheet. *Case Stud. Therm. Eng.* **2021**, *26*, 101043. [CrossRef]

23. Mishra, A.; Kumar, M. Thermal Performance of MHD Nanofluid Flow Over a Stretching Sheet Due to Viscous Dissipation, Joule Heating and Thermal Radiation. *Int. J. Appl. Comput. Math.* **2020**, *6*, 123. [CrossRef]
24. Rashidi, M.M.; Babu, M.J.; Sandeep, N.; Ali, M.E. MHD Squeezing Flow of Nanofluid between Parallel Plates in the Presence of Aligned Magnetic Field. *J. Comput. Theor. Nanosci.* **2016**, *13*, 8700–8708. [CrossRef]
25. Ullah, I.; Ullah, R.; Alqarni, M.S.; Xia, W.-F.; Muhammad, T. Combined Heat Source and Zero Mass Flux Features on Magnetized Nanofluid Flow by Radial Disk with the Applications of Coriolis Force and Activation Energy. *Int. Commun. Heat Mass Transf.* **2021**, *126*, 105416. [CrossRef]
26. Sharma, R.; Hussain, S.M.; Raju, C.S.K.; Seth, G.S.; Chamkha, A.J. Study of Graphene Maxwell Nanofluid Flow Past a Linearly Stretched Sheet: A Numerical and Statistical Approach. *Chin. J. Phys.* **2020**, *68*, 671–683. [CrossRef]
27. Ge-Jile, H.; Shah, N.A.; Mahrous, Y.M.; Sharma, P.; Raju, C.S.K.; Upddhya, S.M. Radiated Magnetic Flow in a Suspension of Ferrous Nanoparticles over a Cone with Brownian Motion and Thermophoresis. *Case Stud. Therm. Eng.* **2021**, *25*, 100915. [CrossRef]
28. Raju, C.S.K.; Ibrahim, S.M.; Anuradha, S.; Priyadharshini, P. Bio-Convection on the Nonlinear Radiative Flow of a Carreau Fluid over a Moving Wedge with Suction or Injection. *Eur. Phys. J. Plus* **2016**, *131*, 409. [CrossRef]
29. Ullah, I.; Alghamdi, M.; Xia, W.F.; Shah, S.I.; Khan, H. Activation Energy Effect on the Magnetized-Nanofluid Flow in a Rotating System Considering the Exponential Heat Source. *Int. Commun. Heat Mass Transf.* **2021**, *128*, 105578. [CrossRef]
30. Nandeppanavar, M.M.; Vaishali, S.; Kemparaju, M.C.; Raveendra, N. Theoretical Analysis of Thermal Characteristics of Casson Nano Fluid Flow Past an Exponential Stretching Sheet in Darcy Porous Media. *Case Stud. Therm. Eng.* **2020**, *21*, 100717. [CrossRef]
31. Shah, Z.; Dawar, A.; Islam, S.; Khan, I.; Ching, D.L.C. Darcy-Forchheimer Flow of Radiative Carbon Nanotubes with Microstructure and Inertial Characteristics in the Rotating Frame. *Case Stud. Therm. Eng.* **2018**, *12*, 823–832. [CrossRef]
32. Shafiq, A.; Rasool, G.; Khalique, C.M. Significance of Thermal Slip and Convective Boundary Conditions in Three Dimensional Rotating Darcy-Forchheimer Nanofluid Flow. *Symmetry* **2020**, *12*, 741. [CrossRef]
33. Ahmad, S.; Ali, K.; Rizwan, M.; Ashraf, M. Heat and Mass Transfer Attributes of Copper–Aluminum Oxide Hybrid Nanoparticles Flow through a Porous Medium. *Case Stud. Therm. Eng.* **2021**, *25*, 100932. [CrossRef]
34. Mishra, A.; Kumar, M. Numerical Analysis of MHD Nanofluid Flow over a Wedge, Including Effects of Viscous Dissipation and Heat Generation/Absorption, Using Buongiorno Model. *Heat Transf.* **2021**, *50*, 8453–8474. [CrossRef]
35. Yaseen, M.; Rawat, S.K.; Kumar, M. Cattaneo–Christov Heat Flux Model in Darcy–Forchheimer Radiative Flow of MoS_2–SiO_2/Kerosene Oil between Two Parallel Rotating Disks. *J. Therm. Anal. Calorim.* **2022**, *147*, 10865–10887. [CrossRef]
36. Ullah, I.; Hayat, T.; Aziz, A.; Alsaedi, A. Significance of Entropy Generation and the Coriolis Force on the Three-Dimensional Non-Darcy Flow of Ethylene-Glycol Conveying Carbon Nanotubes (SWCNTs and MWCNTs). *J. Non-Equilib. Thermodyn.* **2022**, *47*, 61–75. [CrossRef]
37. Hayat, T.; Ullah, I.; Alsaedi, A.; Momani, S. Entropy Optimization in Nonlinear Mixed Convective Flow of Nanomaterials through Porous Space. *J. Non-Equilib. Thermodyn.* **2021**, *46*, 191–203. [CrossRef]
38. Li, Y.M.; Ullah, I.; Alam, M.M.; Khan, H.; Aziz, A. Lorentz Force and Darcy-Forchheimer Effects on the Convective Flow of Non-Newtonian Fluid with Chemical Aspects. *Waves Random Complex Media* **2022**. [CrossRef]
39. Ullah, I. Activation Energy with Exothermic/Endothermic Reaction and Coriolis Force Effects on Magnetized Nanomaterials Flow through Darcy–Forchheimer Porous Space with Variable Features. *Waves Random Complex Media* **2022**. [CrossRef]
40. Ahmad, S.; Farooq, M.; Javed, M.; Anjum, A. Slip Analysis of Squeezing Flow Using Doubly Stratified Fluid. *Results Phys.* **2018**, *9*, 527–533. [CrossRef]
41. Devi, S.P.A.; Devi, S.S.U. Numerical Investigation of Hydromagnetic Hybrid Cu Al_2O_3/Water Nanofluid Flow over a Permeable Stretching Sheet with Suction. *Int. J. Nonlinear Sci. Numer. Simulat.* **2016**, *17*, 249–257. [CrossRef]
42. Upadhya, M.S.; Raju, C.S.K. Implementation of Boundary Value Problems in Using MATLAB®. In *Micro and Nanofluid Convection with Magnetic Field Effects for Heat and Mass Transfer Applications Using MATLAB*; Elsevier: Amsterdam, The Netherlands, 2022; pp. 169–238. [CrossRef]
43. Ahmad, S.; Nadeem, S. Thermal Analysis in Buoyancy Driven Flow of Hybrid Nanofluid Subject to Thermal Radiation. *Int. J. Ambient Energy* **2020**. [CrossRef]
44. Hayat, T.; Sajjad, R.; Alsaedi, A.; Muhammad, T.; Ellahi, R. On Squeezed Flow of Couple Stress Nanofluid between Two Parallel Plates. *Results Phys.* **2017**, *7*, 553–561. [CrossRef]